Geophysical Research Letters

RESEARCH LETTER
10.1029/2024GL113068

The 3D Dynamics of a Wildfire Plume Extending Across the Top of the Planetary Boundary Layer Using an Airborne Doppler Lidar

E. J. Strobach[1,2], S. Baidar[1,2], B. J. Carroll[1,2], and W. A. Brewer[2]

[1]Cooperative Institute for Research in Environmental Sciences, University of Colorado Boulder, Boulder, CO, USA, [2]Chemical Sciences Laboratory, National Oceanic and Atmospheric Administration, Boulder, CO, USA

Key Points:

- Airborne Doppler lidars are ideal for sampling wildfire plumes across the boundary layer
- Strategic sampling from an airborne platform can reveal mechanisms responsible for plume evolution and development
- Increased profile measurement density enables analyses of the fire-modified wind structure

Correspondence to:

E. J. Strobach,
estrobac@umd.edu

Citation:

Strobach, E. J., Baidar, S., Carroll, B. J., & Brewer, W. A. (2025). The 3D dynamics of a wildfire plume extending across the top of the planetary boundary layer using an airborne doppler lidar. *Geophysical Research Letters*, *52*, e2024GL113068. https://doi.org/10.1029/2024GL113068

Received 16 OCT 2024
Accepted 7 APR 2025

Author Contributions:

Conceptualization: E. J. Strobach
Data curation: W. A. Brewer
Formal analysis: E. J. Strobach
Investigation: E. J. Strobach
Methodology: E. J. Strobach
Visualization: E. J. Strobach, S. Baidar, B. J. Carroll
Writing – original draft: E. J. Strobach
Writing – review & editing: S. Baidar, B. J. Carroll

Abstract As wildfire pervasiveness increases with a changing climate, there is a need to develop new techniques with emerging technologies to understand the interaction between wildfires and the surrounding atmosphere at a high spatiotemporal resolution. The Fire Influence on Regional to Global Environments and Air Quality (FIREX-AQ) experiment conducted in 2019 focused on wildfires using several measurement platforms aboard aircraft. In this study, we interpret wind measurements across a smoke plume transported vertically and advected along the top of the boundary layer (BL) from an airborne Doppler lidar (DL). Flight transects parallel and perpendicular to the orientation of the plume enabled the characterization of key features such as a fire-induced spanwise vortex, large downdrafts that modified the smoke plume, and the evolving velocity structure at different distances downwind of the fire-induced convergence zone (FICZ) at an unprecedented horizontal and vertical resolution of 10s of meters.

Plain Language Summary Observations of wildfire dynamics are key in understanding how fires evolve and interact with the surrounding atmosphere. Using Doppler lidars (DL) aboard aircraft allow high resolution measurements of winds that elucidate the interactions responsible for the development of wildfire smoke plumes. The following study interrogates 3D wind data collected over a fire using a unique flight strategy, and identifies key features responsible for plume dynamics at different distances away from the fire.

1. Introduction

The use of Doppler lidars (DLs) to study fire behavior was first demonstrated by Banta et al. (1992) using a combination of fixed azimuth and fixed elevation angle scans to characterize the flow structure of a smoke plume over a region of convergence that resembled a type II vortex described in McRae and Flannigan (1990). Only a handful of studies featuring Doppler lidars (DLs) in the years following Banta et al. (1992) focused on the dynamical evolution of the plume from a fixed point (e.g., Bozier et al., 2007). It was not until the early 2010s that DLs were integrated into field studies focused on fire behavior, in part because of a wider acceptance of DLs as a reliable remote sensing instrument, but also because of increased wildfire pervasiveness.

Charland and Clements (2013) examined the development of a smoke plume from a prescribed burn on a slope using a stationary scanning DL and noted the importance of convergent flow at the edge of the plume as a primary contributor to plume development. The introduction of mobile DLs enabled analyses of the kinematic and thermodynamic characteristics of smoke outflows during propagation (Lareau & Clements, 2015). The appeal of mobile DLs over stationary DLs was further demonstrated during the Rapid Deployments to Wildfires Experiment (RaDFIRE) targeting fire-modified winds and smoke laden boundary layers (BL) from the ground during transient events (Clements et al., 2018).

While stationary and ground-based mobile DLs improved the understanding of the dynamics driving fire spreading conditions, challenges still remained when characterizing the spatial structure of smoke plumes and fire-induced updrafts in complex terrain. The use of an airborne DL during the 2019 Fire Influence on Regional to Global Environments and Air Quality (FIREX-AQ) led to the isolation of fire-induced updrafts and their dynamical properties (Strobach et al., 2023). The California Fire Dynamics Experiment (CalFiDE) of 2022 that followed FIREX-AQ featured the deployment of several mobile ground-based systems as well as an aircraft with remote sensing capability (Carroll et al., 2024). Strobach et al. (2024) examined one of the fires surveyed during

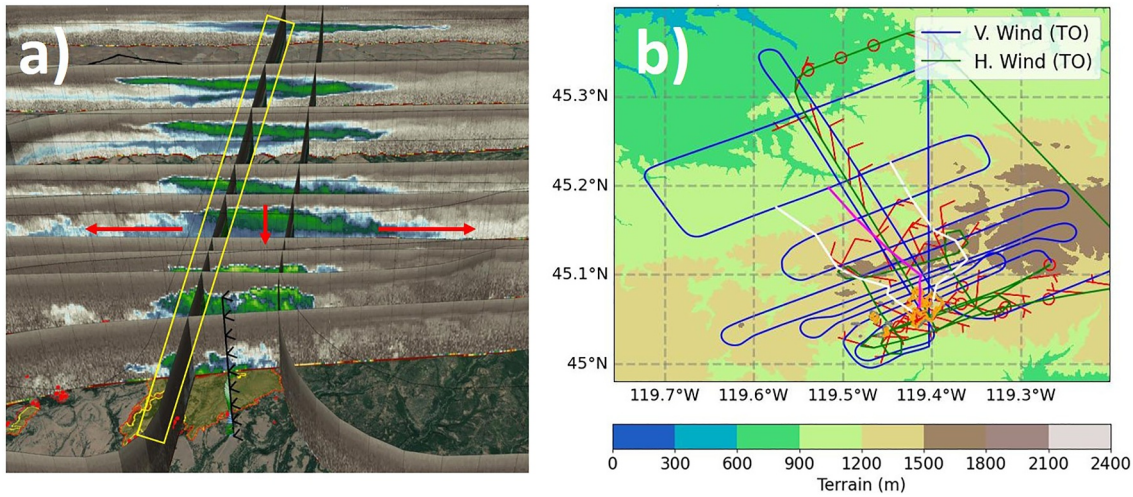

Figure 1. (a) Image of smoke backscatter along transects perpendicular to plume orientation overlaid with transects parallel to plume orientation, and a, b) top view of the entire flight plan color-coded by mode of operation (vertical stares–blue or conical scans–green). Overlaid in (a) is a horizontal wind vector profile upwind of the fire perimeter shown by yellow, orange, and red contour lines along terrain at the base of the foremost perpendicular transect. Annotations in (a) include a yellow box to highlight the parallel transect examined in Section 3.1, and red arrows denoting smoke outflow and downward motion from the center of the plume as discussed in Section 3.2. Near-surface winds (red barbs), the approximate width and centerline of the plume (white and magenta lines), the fire perimeter, and terrain (shading) are overlaid in (b).

CalFiDE, and analyzed the time evolution of a buoyant plume jet, the fire-induced inflow leading up the updraft, and lateral and plume-top entrainment using data from an airborne DL.

The smaller-scale dynamics related to entrainment and fire-atmosphere feedback investigated in Strobach et al. (2023, 2024) remain challenging from a modeling standpoint and require further investigation (Sokolik et al., 2019). To address this, we interrogate data collected during FIREX-AQ to investigate the 3D dynamics of a smoke plume along the top of the BL over the 163 Complex Fire near Medford, Oregon. The flight strategy and methods developed to analyze the 3D flow structure is presented in Section 2; details about the DL used for this study and the products available can be found in related works (e.g., Carroll et al., 2024; Schroeder et al., 2020; Strobach et al., 2023), and thus will not be discussed. An analysis of the spanwise structure of the smoke plume in the direction of propagation, horizontal wind measurements upwind and downwind of the firefront, and the development of relatively strong downdrafts downwind of fire is presented in Section 3. Conclusions are presented in Section 4.

2. Methods

2.1. Flight Strategy

Figure 1 shows the flight strategy over the 163 HK Complex fire between 17:40 and 20:00 UTC on 9 August 2019. Multiple transects flown parallel and perpendicular to the plume were conducted to characterize along-wind transport and the expansion and evolution of smoke along a Lagrangian path, respectively. Transects along the perimeter of the fire were also conducted to identify fire-induced inflow. Plume perpendicular transects and two plume-parallel transects were conducted when the DL was configured to measure vertical winds. A separate plume-parallel transect and transects surveying the perimeter of the fire were conducted when the DL was configured to measure horizontal winds. Vertical winds were measured between 17:40 and 19:00 UTC while horizontal winds were measured between 19:00 and 20:00 UTC. Both modes of operation relied on the presence of aerosol for signal. Data presented in this study were filtered out in situations where the signal was suboptimal. Further details about the time difference between horizontal and vertical winds for plume-parallel transects is left for the next subsection. Other features in Figure 1 not discussed in this section are referenced when discussing results.

2.2. Plane-Oriented Winds and Higher Order Calculations

The collocation of vertical and horizontal wind measurements oriented along the plume direction allowed the derivation of winds parallel and perpendicular to the transect following Strobach et al. (2023) as shown vectorially by Equation 1

$$\left(v_{\parallel}, v_{\perp}\right) = \left(\vec{v} \cdot \hat{h}_m, \vec{v} \times \hat{h}_m\right) \tag{1}$$

where $v_{\parallel}$ and $v_{\perp}$ are the parallel and perpendicular winds, and $\hat{h}_m$ is the direction of the aircraft adjusted to meteorological coordinates (i.e., $\hat{h}_m = \hat{h} + 180$). Combining the horizontal and vertical wind measurements allowed streamlines to be constructed after the data was placed into a rectangular grid. Defining a rectangular grid required vertical and horizontal interpolation of both vertical and horizontal winds. We considered 50 m for the vertical interpolation (≈ along-beam resolution of DL) and the median difference in horizontal distance between vertical velocity profiles (≈10 m) along the flight track for horizontal interpolation. The fine-scale interpolation was chosen despite the 1.5 km spacing between horizontal wind measurements since consecutive horizontal wind measurements were not drastically different on average.

Since the w and $v_{\parallel}$ are defined on a rectangular grid, we can now derive quantities related to fluid flow on the observation plane. Here, we define Equations 2 and 3 as

$$\eta = \frac{\partial w}{\partial x} - \frac{\partial v'_{\parallel}}{\partial z} \tag{2}$$

$$Div = \frac{\partial v'_{\parallel}}{\partial x} + \frac{\partial w}{\partial z} \tag{3}$$

where η and Div represent vorticity and divergence on the observation plane, respectively. The prime in $v_{\parallel}$ represents perturbations in $v_{\parallel}$ after the plane-averaged horizontal winds are removed via Equation 4

$$v'_{\parallel} = v_{\parallel} - \langle v_{\parallel} \rangle \tag{4}$$

Other techniques for joining wind components to calculate Equations 2 and 3 have been developed, such as the one described in Guo et al. (2023); however, we elected to adopt the approach outlined above since the analysis was done with evenly spaced data on a rectangular grid while the method employed by Guo et al. (2023) was developed for irregularly spaced data.

To ensure that the plume structure did not change significantly between vertical and horizontal wind profile measurements, we compare vertical velocity profiles collocated in space that were separated in time by grouping profiles where the plume-parallel transect intersected plume-perpendicular transects. Figure 2 shows collocated vertical velocity profiles spanning the upwind and downwind regions of the fire over a horizontal distance of 17 km relative to the base of the plume (first eight transects in Figure 1a and vertical magenta dashed lines in Figure 3). The magnitude and profile structure of vertical velocity, especially over and near the fire, was very similar between transects, thus indicating that the conditions were approximately stationary within that time frame. The variability of vertical velocity measurements was slightly greater for plume-perpendicular measurements (shown in red) compared to plume-parallel measurements (shown in black), with the largest horizontal bars spanning 1 m s^{-1}. The relatively small time separation between horizontal and vertical wind profiles of an hour or less, the overall agreement in the vertical velocity structure between plume-parallel and plume-perpendicular transects, and the frequent overlap of horizontal bars between profiles is believed to be sufficient for a semi-quantitative analysis.

3. 163 HK Complex Fire

3.1. Observations Parallel to Plume Orientation

Figure 3 shows the plume-parallel transect farthest to the west outlined by the yellow box in Figure 1a with the height coordinate shifted relative to plume base at the 0-km location on the x-axis. Vertical velocities in Figure 3a

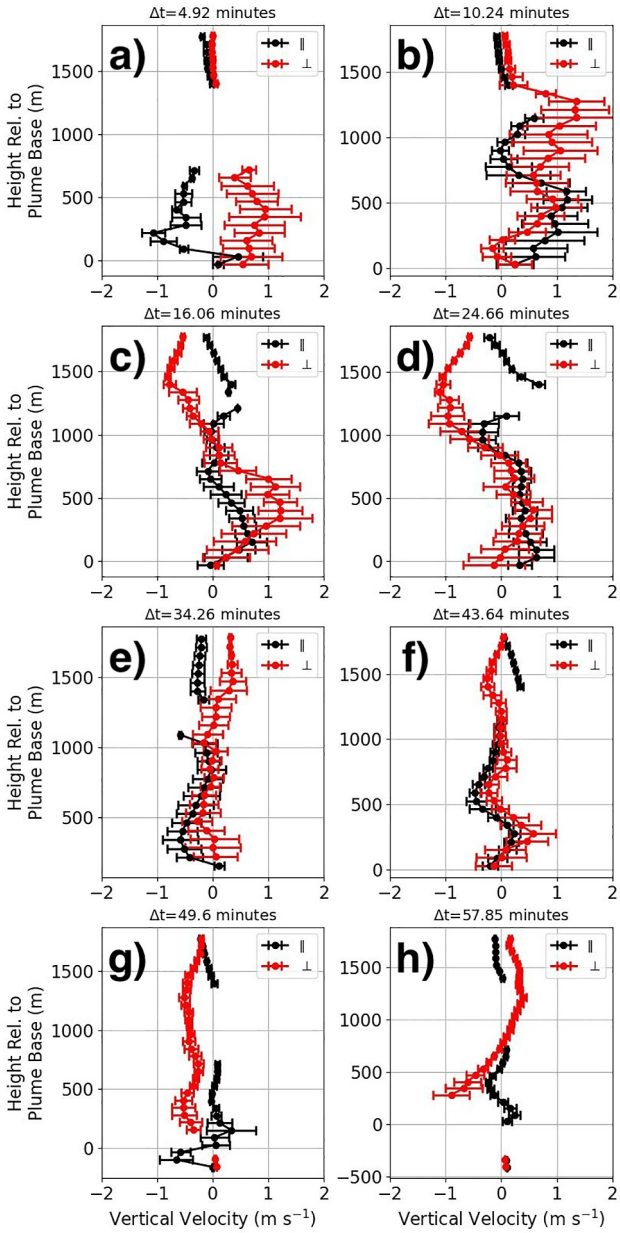

Figure 2. Comparison between collocated vertical velocity profiles where the plume-parallel transect (black–||) intersects with plume-perpendicular transects (red–⊥) at heights relative to plume base. (a–h) represent profiles at the location of the first eight plume-perpendicular transects in Figure 1a, with (a) being the closest transect to the foreground and (h) being the second-most distant plume-perpendicular transect intersecting the plume-parallel transect. The time difference between collocated plume-parallel and plume-perpendicular profiles is included in the title of each subplot. The horizontal bars represent the standard deviation of 20 profiles grouped across both transects, which represents about a distance of 200 m across the intersection for both plume parallel and perpendicular directions. The time difference between profiles ranged from 5 min to an hour, and the vertical winds were chosen over the horizontal winds due to low profile density of the latter.

are strongest and deepest between distances 0 and 3 km. The strongest updraft at 0 km coincides with enhanced smoke backscatter from the surface to the top of the plume in Figure 3b, and is believed to be the location of active burning. The lofted smoke plume advected to the northwest has a thickness of about 650 m until a distance 5 km downwind, where the smoke plume appears to dilute and reduce in thickness upon crossing a ridge (approximately the location of the 5th plume-perpendicular transect). The transition from a thick and opaque plume to a thin and diluted plume occurs following a transition from upward to downward motion. Closer inspection of smoke backscatter in Figure 3b at the location of downward motion reveals a brief increase in plume thickness toward the surface that is suggestive of downward transport. Downwind of the ridge at 5 km, the vertical velocity significantly reduces while the plume becomes increasingly thinner and increases in smoke backscatter. In other words, the smoke is confined and does not disperse efficiently, thus leading to an increase in smoke backscatter farther downwind.

3.1.1. Streamline Structure, Vorticity and Divergence

The streamline structure in Figures 3a, 3c and 3d between 0 and 12 km reveals clockwise (CW) vorticity ranging from −0.01 and −0.03 s^{-1} (Figure 3c) that is similar in magnitude to spanwise vortices observed in Hill et al. (2010) when examining mountain rotors. The main vortex (MV) located immediately downwind of 0 km is about 5 km wide and 1 km deep. The horizontal wind across the upper portion of the MV is from the east-to-southeast in the direction of plume orientation (Figure 1b), and thus results in the horizontal orientation of streamlines at the top of the plume as vertical motion reduces. Near-surface winds transition from southeasterly to northeasterly in the direction of the MV across the fire-induced convergence zone (FICZ) centered at 0 km (refer to green arrows in Figure 3a). Flow splitting within the downturning portion of the MV exhibited in streamlines toward the surface and FICZ highlights recirculation influenced by fire-induced inflow. Across the MV is enhanced convergence (−0.15 s^{-1}) and divergence (0.2 s^{-1}) within the upturning and downturning branches of the vortex, respectively. Enhanced convergence/divergence elsewhere occur within the FICZ as a result of complex flow conditions and enhanced vertical motion. The combination of vector shear and fire-induced buoyancy represent the mechanisms of convective overturning and vortex generation associated with the MV, while the vortices depicted by streamlines immediately downwind of the MV occur as the plume decreases in depth and smoke backscatter. The vortices that emanate and break off from the MV advect and dissipate from the FICZ while becoming progressively smaller in the presence of reduced vertical motion.

In addition to CW flow associated with vortices generated and advected from the FICZ across 0–12 km are counter-clockwise (CCW) flows across the upwind edge of the plume toward the FICZ and within shallow layers near the surface in Figures 3a and 3c that approximate 250 m in depth. The CCW flow upwind of the FICZ is a result of southeasterlies merging with downward motion and into a region of upward motion over the active burn area between −2 and 0 km as supported by positive vorticity in Figure 3c. The positive vorticity near the surface, particularly downwind of the FICZ, is a result of fire-induced inflow and the accompanying wind shear structure (i.e., Figure 4b) that dominates the vorticity calculation in Equation 2. Enhance-

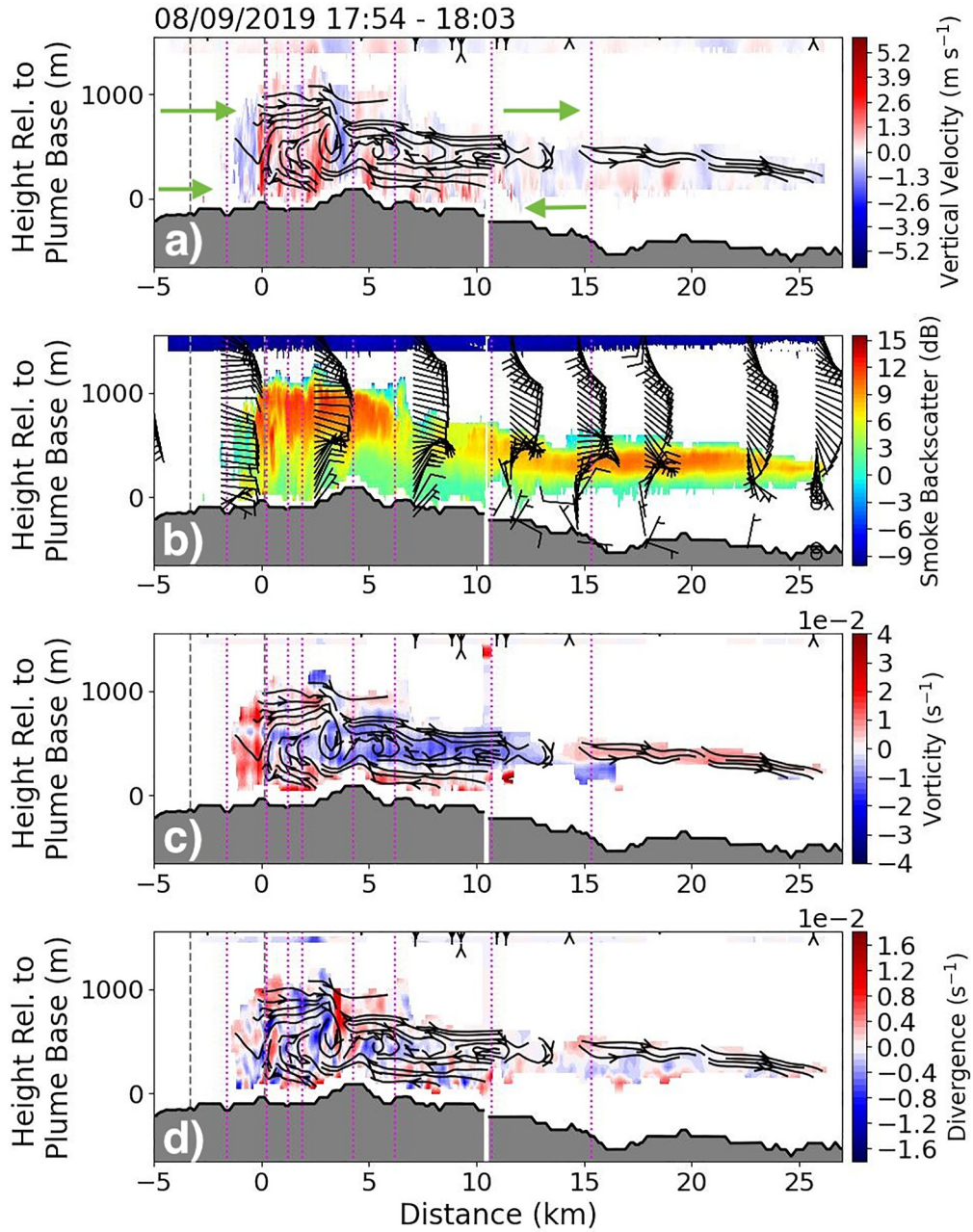

Figure 3. (a) Vertical velocity overlaid with streamlines, (b) smoke backscatter overlaid with Earth-relative wind barbs, and (c) vorticity and (d) divergence overlaid with streamlines at heights relative to plume base. The pink dotted lines represent the position of the perpendicular flight transects shown in Figure 1a, while the gray dashed lines approximate the fire perimeter bounds along the plume-parallel transect. Green arrows show the general horizontal flow structure upwind and downwind of the fire, and correspond to in-plane parallel wind profiles in Figures 4a and 4b. The wind barbs are plotted with a reduced density so as not to overwhelm the figure.

ments in convergence and divergence are noted within the shallow inflow layer, which is likely related to flow accelerations across complex terrain and localized enhancements in vertical motion as evident in Figure 3a.

3.1.2. Flow Convergence Into the Firefront

In order to further evaluate the role of fire-modified winds on the dynamics of the MV centered over the FICZ, we examine the winds rotated parallel and perpendicular to the flight transect outlined by the yellow box in Figure 1a

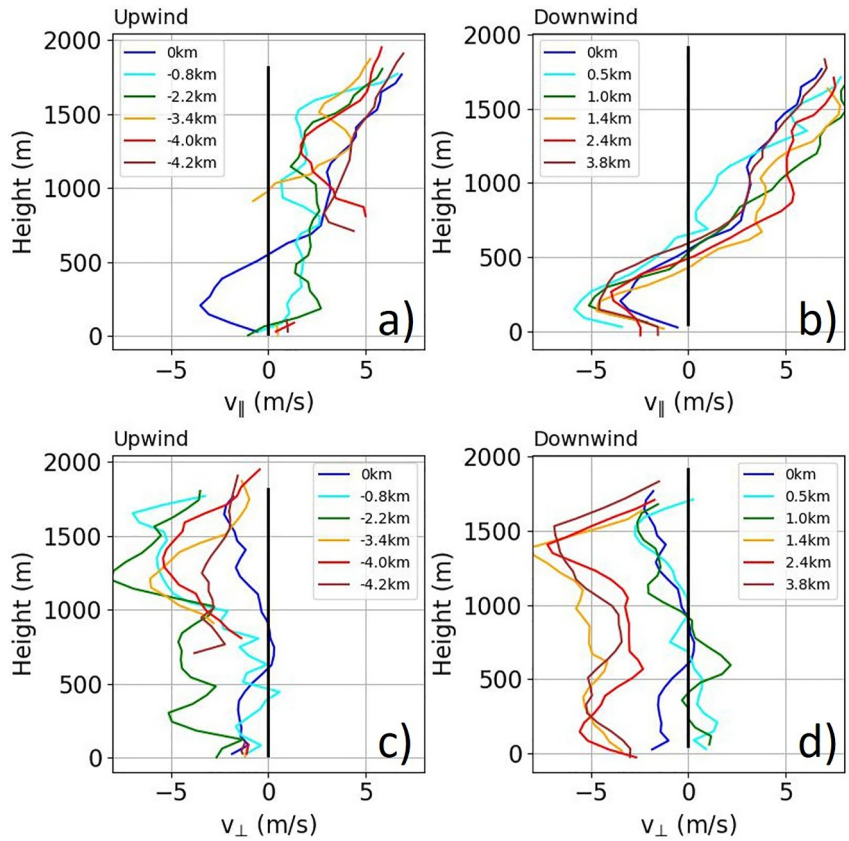

Figure 4. Winds parallel to the observation plane (a) upwind–left and (b) downwind–right of the fire and winds perpendicular to the observation plane (c) upwind–left and (d) downwind–right at heights above ground level (AGL). Profiles indicate different distances from the profile closest the active burn area, where negative and positive distances represent upwind and downwind, respectively, and the profile at 0 km represents a horizontal wind measurement approximately located at the burn area. Vertical black lines in plots are included to delineate between negative and positive winds.

at varied distances upwind and downwind of the FICZ. Figures 4a–4d represent winds parallel and perpendicular to the plume-parallel transect upwind (left panels–negative distance on *x*-axis in Figure 3) and downwind (right panels–positive distances on *x*-axis in Figure 3) of the fire at heights above ground level (AGL). Included in each panel is a horizontal wind profile in blue that is approximately collocated with the FICZ. With the exception of the profile over the FICZ, winds parallel to the orientation of the plume flow uniformly toward the fire from the upwind direction and increase with height. A weak wind maximum near the surface is observed −2.2 km (upwind) from the FICZ that matches the height of the opposing wind maximum at the FICZ (0 km, blue profile). Winds perpendicular to the plume-parallel transect flow from the east and generally weaken with proximity to the FICZ, especially near the surface. The reduction in winds is likely the result of horizontal inflow converting into vertical motion over the fire perimeter. This is corroborated by the streamline structure and vorticity field in Figure 3c between −2 and 0 km as discussed in the previous subsection.

While parallel winds above 500 m are similar upwind (Figure 4a) and downwind (Figure 4b)–namely, winds uniformly flow from upwind and increase with height–winds near the surface (below 500 m) flow toward the FICZ from downwind and therefore exhibit an opposite sign (negative parallel winds) relative to near-surface winds upwind of the fire. All downwind profiles in Figure 4b feature a near-surface wind maximum at a height of about 250 m. The winds strengthen toward the fire from downwind by 2–3 m s^{-1} over 2 km (refer to profiles spanning maroon to cyan in Figure 4b) to a maximum of about 6 m s^{-1}. The opposing flow structure on either side of the FICZ near the surface is indicative of inflow into the fire and coincides with positive vorticity near the surface in Figure 3c. The downwind perpendicular wind component in Figure 4d is nearly uniform and from the east, but with a marked decrease close to the FICZ. The simultaneous weakening of $v_\perp$ and strengthening

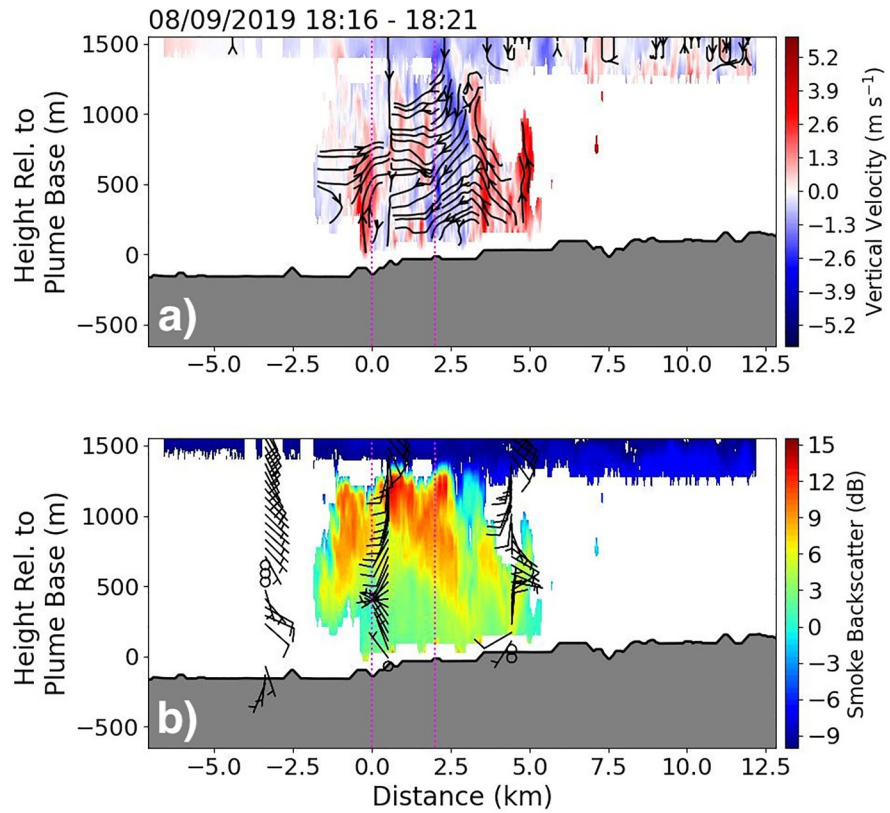

Figure 5. (a) Vertical velocity overlaid with streamlines and (b) smoke backscatter overlaid with Earth-relative wind barbs for the 3rd plume-perpendicular transect from the foreground in Figure 1a (third dashed line in Figure 3). The magenta dotted lines represent plume-parallel transects, with the dotted line centered on 0 km representing the transect analyzed in Figure 3.

of $v_{\parallel}$ could be a result of winds rotating perpendicular to the FICZ as heat from the fire draws air inward, or as some of the horizontal momentum gets converted to vertical momentum via fire-induced buoyancy.

The convergence into an active burn area near the surface is believed to support the development of the MV between 0 and 5 km. The development of strong downward motion within the downturning portion of the MV coincides with several plume-perpendicular transects in Figure 1a featuring lateral spreading of smoke as depicted by the vertical narrowing and horizontal elongation of the plume. The narrowing and elongation of the plume is observed starting at the location of the 5th plume-perpendicular transect (Figures 1a and 5th magenta line in Figure 3), which is coincident with the downturning portion of the MV. The lateral spreading of the smoke (Figure 1a) leads to a detached plume hovering at BL top that advects downwind in a region of quiescent vertical motion as discussed in Section 3.1. To understand the dynamics of the plume perpendicular to the propagation direction, we now examine the flow structure across a plume-perpendicular transect oriented from southwest to northeast.

3.2. Dynamics Perpendicular to Plume Orientation

A substantial change in the plume morphology is demonstrated by plume widening over a short horizontal distance (white plot lines in Figure 1b) and the spreading of smoke from the plume center (red arrows in Figure 1a). Figure 1a indicates the 5th plume-perpendicular transect as representing the location where a dynamical transition took place. The location of the 5th plume-perpendicular transect is approximately collocated with the downturning portion of the MV centered over the fire as discussed in Figure 3. However, it turns out that enhanced downward motion was observed in the 3rd and 4th plume-perpendicular transects northeast of the plume-parallel transect investigated in the previous section (i.e., the plume-parallel transect centered at 0 km in Figure 5). For this reason, we examine the 3rd in detail below, which represents the first plume-perpendicular transect where strong downward motion was observed that also happens to be located near the FICZ.

Figure 5 shows vertical velocity (a) and smoke backscatter (b) along the 3rd plume-perpendicular transect from the foreground in Figure 1a at heights above plume base. At the center of Figure 5a is a relatively strong downdraft (maximum downdraft strength ≈4.5 m s^{-1}) that is 2.5 km in diameter. On either side of the downdraft are updrafts of comparable width extending across a depth between 1 and 1.5 km, with local enhancements in updraft velocity exceeding 4 m s^{-1}. The updraft to the southwest (left) of the strong downdraft overlaps with the plume-parallel transect discussed in Section 3.1 (note the magenta dotted line at 0 km in Figure 5), which, based on Figure 3a, coincides with a region of enhanced upward motion associated with upturning portion of the MV. Most of the smoke aerosol in Figure 5b occupies the top of the plume between −2 and 4.5 km. Local enhancements in smoke aerosol along the top of the plume is observed at three locations: southwest of the center wind barb profile in Figure 5b (near 0.5 km), northeast of the center wind profile between 0.5 and 3 km, and near 4.5 km southwest of the wind barb profile farthest to the northeast. The location of enhanced smoke aerosol coincides with relatively strong updrafts and a downdraft across the depth of the plume to the surface, and underscore the importance of transport dynamics responsible for distributing smoke aerosol.

The streamlines in Figure 5a combine the vertical and horizontal winds along the observation plane as done in Section 3.1. There is a reduced number of horizontal wind profiles, which requires caution when analyzing the streamline structure. Nevertheless, the fire-induced updraft at 0 km that overlaps with the plume-parallel transect investigated in the previous section appears responsible for transporting smoke upwards and to the northeast along streamlines. A marked transition in the plane-parallel structure is observed at 0 km at near center wind barb profile in Figure 5b. The winds across the first 1 km from the surface associated with the wind barb profile near 0 km flows from the northwest, which approximately lines up with the orientation of the plume but in the opposite direction. Thus, because the plane-parallel wind is negligible near 0 km, then interpolations will be heavily weighted by horizontal wind profiles at the edges in Figure 5b. As a result, winds appear to flow from the northeast at distances greater than 2.5 km. The streamlines along the downdraft are predominately downward near the top (stronger downward motion) before sloping to the southwest toward the surface along the axis of the downdraft. The smoke at the top of the downdraft slopes along streamlines, but closer to the surface, the streamlines transition from enhanced smoke to less concentrated smoke. This appears opposite to what is observed in the smoke backscatter, which slopes northeast to the surface in the downdraft region. Though it would seem plausible that enhanced smoke follows the direction of streamlines, we cannot rule out the role of dynamics and the distribution of smoke outside of the observation plane. Streamlines along the updraft to the northeast slope upwards to the southwest, which aligns with the orientation of locally enhanced smoke that spans the top half of the updraft.

4. Conclusions

In this study, we analyzed a wildfire plume using an airborne DL with a flight strategy that included transects parallel and perpendicular to plume orientation. Analyses parallel to the plume revealed the development of a spanwise vortex over the fire-induced convergence zone (FICZ) that spanned the depth of the plume and advected vorticity downwind that subsequently dissipated. This was made possible using spatially collocated vertical and horizontal wind profiles that were measured separately in time as supported by analyses revealing quasi-stationary conditions between vertical wind profile measurements where plume-perpendicular transects intersected the plume-parallel transect investigated. The time difference between vertical velocity profiles where plume-parallel and plume-perpendicular transects intersected ranged between 5 min to and hour, which encompassed the time it would take for vorticity to be advected from the fire source to 10 km downwind where vortices completely dissipated (i.e (10–3 km)/3 m s^{-1} → 40 min, where 3 m s^{-1} approximately represents the wind magnitude of parallel winds at the height of the vortex layer).

The spanwise vorticity within the vortex layer extending from the main vortex (MV) was comparable in magnitude to what has been observed in mountain rotors. Regions of positive vorticity either coincided with horizontal winds transitioning from a downdraft into an updraft (upwind of the FICZ) or as a result of the vertical wind shear of plane-parallel winds dominating the vorticity calculation in regions of reduced vertical motion (fire-modified inflow layer downwind of the FICZ). Convergence was most prominent over the updraft region near the FICZ, while enhanced divergence was observed within the downturning portion of the MV. The convergent flow on either side of the FICZ appeared important in generating vertical convergence spanning the width of the MV.

The background winds at plume-top and fire-induced inflows into the FICZ from downwind are important mechanisms leading to the convective overturning of the plume.

Directly downwind of the MV was a substantial change in the plume morphology that coincided with the lateral spreading of smoke and enhanced downward motion. Close examination of plume-perpendicular transects revealed strong downdrafts that developed near the FICZ that was northeast of the plume-parallel transect investigated. These downdrafts were comparable in strength to neighboring updrafts, and extended above the height of the plume. The lack of alignment between the downturning portion of the spanwise vortex along the plume-parallel transect and the strong and large downdrafts within the FICZ region points to a complex vorticity structure whose 3D projection cannot be mapped completely by conducting single transects alone.

Data Availability Statement

Data from the Doppler lidar during FIREX-AQ can be requested and accessed through the following link: https://csl.noaa.gov/groups/csl3/measurements/2019firex-aq/.

Acknowledgments
The authors would like to thank the reviewers for feedback on the manuscript, and to acknowledge the data collection and curating efforts by personnel at the Chemical Sciences Laboratory that made this study possible. This work will be paid for by the Cooperative Institute for Research In Environmental Sciences (CIRES) as part of work that was carried out in FIREX-AQ.

References

Banta, R., Olivier, L., Holloway, E., Kropfli, R., Bartram, B., Cupp, R., & Post, M. (1992). Smoke-column observations from two forest fires using Doppler Lidar and Doppler radar. *Journal of Applied Meteorology and Climatology*, *31*(11), 1328–1349. https://doi.org/10.1175/1520-0450(1992)031<1328:scoftf>2.0.co;2

Bozier, K., Pearson, G., & Collier, C. (2007). Doppler Lidar observations of Russian forest fire plumes over Helsinki. *Weather*, *62*(8), 203–208. https://doi.org/10.1002/wea.48

Carroll, B. J., Brewer, W. A., Strobach, E., Lareau, N., Brown, S. S., Valero, M. M., et al. (2024). Measuring coupled fire-atmosphere dynamics: The California fire dynamics experiment (Calfide). *Bulletin of the American Meteorological Society*, *105*(3), E690–E708. https://doi.org/10.1175/bams-d-23-0012.1

Charland, A., & Clements, C. (2013). Kinematic structure of a wildland fire plume observed by Doppler Lidar. *Journal of Geophysical Research: Atmospheres*, *118*(8), 3200–3212. https://doi.org/10.1002/jgrd.50308

Clements, C. B., Lareau, N. P., Kingsmill, D. E., Bowers, C. L., Camacho, C. P., Bagley, R., & Davis, B. (2018). The Rapid Deployments to Wildfires Experiment (RADFIRE): Observations from the fire zone. *Bulletin of the American Meteorological Society*, *99*(12), 2539–2559. https://doi.org/10.1175/bams-d-17-0230.1

Guo, X., Guo, J., Zhang, D.-L., & Yun, Y. (2023). Vertical divergence profiles as detected by two wind-profiler Mesonets over east China: Implications for nowcasting convective storms. *Quarterly Journal of the Royal Meteorological Society*, *149*(754), 1629–1649. https://doi.org/10.1002/qj.4474

Hill, M., Calhoun, R., Fernando, H., Wieser, A., Dörnbrack, A., Weissmann, M., et al. (2010). Coplanar Doppler Lidar retrieval of rotors from t-Rex. *Journal of the Atmospheric Sciences*, *67*(3), 713–729. https://doi.org/10.1175/2009jas3016.1

Lareau, N., & Clements, C. (2015). Cold smoke: Smoke-induced density currents cause unexpected smoke transport near large wildfires. *Atmospheric Chemistry and Physics*, *15*(20), 11513–11520. https://doi.org/10.5194/acp-15-11513-2015

McRae, D., & Flannigan, M. (1990). Development of large vortices on prescribed fires. *Canadian Journal of Forest Research*, *20*(12), 1878–1887. https://doi.org/10.1139/x90-252

Schroeder, P., Brewer, W. A., Choukulkar, A., Weickmann, A., Zucker, M., Holloway, M. W., & Sandberg, S. (2020). A compact, flexible, and robust micropulsed Doppler Lidar. *Journal of Atmospheric and Oceanic Technology*, *37*(8), 1387–1402. https://doi.org/10.1175/jtech-d-19-0142.1

Sokolik, I., Soja, A., DeMott, P., & Winker, D. (2019). Progress and challenges in quantifying wildfire smoke emissions, their properties, transport, and atmospheric impacts. *Journal of Geophysical Research: Atmospheres*, *124*(23), 13005–13025. https://doi.org/10.1029/2018jd029878

Strobach, E., Brewer, W., Senff, C., Baidar, S., & McCarty, B. (2023). Isolating and investigating updrafts induced by wildland fires using an airborne Doppler Lidar during Firex-AQ. *Journal of Geophysical Research: Atmospheres*, *128*(14), e2023JD038809. https://doi.org/10.1029/2023jd038809

Strobach, E., Carroll, B. J., Baidar, S., Brown, S., Ahmadov, R., Brewer, W., et al. (2024). A case study featuring the time evolution of a fire-induced plume jet over the rum creek fire: Mechanisms, processes, and dynamical interplay. *Journal of Geophysical Research: Atmospheres*, *129*(10), e2023JD040483. https://doi.org/10.1029/2023jd040483